

# Video Interpolation via Generalized Deformable Convolution

Zhihao Shi, Xiaohong Liu, *Student Member, IEEE*, Kangdi Shi, Linhui Dai, Jun Chen, *Senior Member, IEEE*

**Abstract**—Video interpolation aims at increasing the frame rate of a given video by synthesizing intermediate frames. The existing video interpolation methods can be roughly divided into two categories: flow-based methods and kernel-based methods. The performance of flow-based methods is often jeopardized by the inaccuracy of flow map estimation due to oversimplified motion models while that of kernel-based methods tends to be constrained by the rigidity of kernel shape. To address these performance-limiting issues, a novel mechanism named generalized deformable convolution is proposed, which can effectively learn motion information in a data-driven manner and freely select sampling points in space-time. We further develop a new video interpolation method based on this mechanism. Our extensive experiments demonstrate that the new method performs favorably against the state-of-the-art, especially when dealing with complex motions.

**Index Terms**—Video interpolation, generalized deformable convolution

## I. INTRODUCTION

Video interpolation is a classic problem in computer vision and has received significant attention in recent years. It aims at increasing the frame rate of a given video by synthesizing intermediate frames while maintaining spatial and temporal consistencies. The existing video interpolation methods can be roughly divided into two categories: flow-based methods and kernel-based methods.

Flow-based methods generate the value of each pixel in the target intermediate frame by finding an associated optical flow. They often suffer from significant artifacts due to inaccurate optical flow estimation. This issue cannot be resolved in a straightforward manner even if convolutional neural networks (CNNs) are employed to (implicitly) estimate flow maps [15], [26], [22]. The traditional flow-based methods typically adopt linear model with the oversimplified assumption of uniform motion between neighboring frames. Recently, a more sophisticated approach is put forward in [39] for estimating motion trajectories, where the naive linear model is replaced by a more accurate quadratic model that can take advantage of latent motion information by simultaneously exploiting four consecutive frames. Nevertheless, it is conceivable that the complexities and irregularities of real-world motions cannot be completely captured by a simple mathematical model. Moreover, the pixel-level displacement performed in flow-based methods is inherently inadequate for handling diffusion

Z. Shi, X. Liu (corresponding author), K. Shi, L. Dai and J. Chen are with the Department of Electrical and Computer Engineering, McMaster University, Hamilton, ON, L8S 4K1, Canada (e-mail: {shiz31, liux173, shik9, dail5}@mcmaster.ca; junchen@ece.mcmaster.ca).

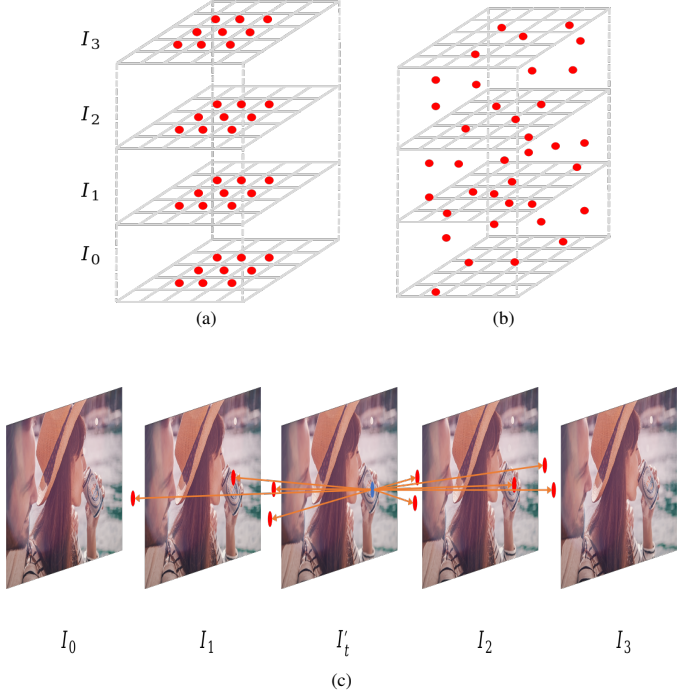


Fig. 1. Illustration of (a) conventional convolution with  $3 \times 3 \times 4 = 36$  sampling points, (b) GDConv with the same number of sampling points, and (c) visualization of interpolating one frame with GDConv.

and dispersion effects, especially when such effects are not negligible on the timescale corresponding to the frame rate.

Kernel-based methods directly generate the target intermediate frame by applying spatially-adaptive convolution kernels to the given frames. They circumvent the need for flow map estimation and consequently are not susceptible to the relevant issues. On the other hand, the rigidity of kernel shape [27], [28] severely limits the types of motions that such methods can handle. Indeed, one may need to choose a very large kernel size to ensure enough coverage, which is highly inefficient. As a partial remedy, [2] proposes adaptive deployment of convolution kernels guided by flow maps; nevertheless, the receptive field is still constrained by predetermined kernel shape. More recently, [19] introduces a new approach known as AdaCoF, which utilizes spatially-adaptive deformable convolution (DConv) to select suitable sampling points needed for synthesizing each target pixel; however, although this approach eliminates the constraint on the kernel shape in the spatial domain, it does not fully exploit the degrees of freedom available in whole space-time.

In summary, flow-based methods and kernel-based methods

have their respective limitations. For flow-based methods, even with the aid of sophisticated mathematical models, flow map estimation is still a challenging task due to the intricacies of inter-frame motion trajectories. For kernel-based methods, predetermined kernel shape lacks the flexibility to cope with a great variety of motions in terms of range and pattern; while recent innovations have alleviated the rigidity issue to a certain extent, much remains to be done.

The main contribution of this paper is a new approach to video interpolation, which overcomes the hurdles of the aforementioned methods and retains their desirable properties. The key mechanism underlying the proposed approach is generalized deformable convolution (GDConv). An illustration of the difference between conventional convolution and our GDConv in terms of the freedom to select sampling points can be found in Fig. 1 (a) and (b). Fig. 1 (c) provides a rough idea of how GDConv can be leveraged for video interpolation: each pixel (e.g., the blue one) in the target intermediate frame is synthesized based on the corresponding sampling points (the red ones). It is worth noting that as the sampling points are allowed to move freely in the continuous space-time, the receptive field of GDConv is basically unconstrained, making it possible to handle all kinds of motions (say, large motions). Moreover, GDConv does not rely on a prescribed mathematical model for motion estimation; instead, it is trained to learn real-world motion trajectories and patterns via a data-driven approach. In our design, GDConv is encapsulated in a generalized deformable convolution module (GDCM). We integrate two GDCMs with several other modules, including the source extraction module (SEM), the context extraction module (CEM) and the post-processing module (PM), to form a generalized deformable convolution network (GDConvNet) for video interpolation. Our extensive experimental results demonstrate that owing to the effective design, the proposed GDConvNet performs favorably against the current state-of-the-art.

## II. GENERALIZED DEFORMABLE CONVOLUTION NETWORK

The overall architecture of GDConvNet is shown in Fig. 3. Given a video clip which consists of  $T + 1$  source frames  $I_0, I_1, \dots, I_T$ , the task of GDConvNet is to synthesize an intermediate frame  $I_t$ ,  $t \in [0, T]$ . To this end, it first generates a GDCM source feature map through SEM and extracts context maps  $C_0, C_1, \dots, C_T$  through CEM from  $I_0, I_1, \dots, I_T$ ; input frames and context maps are then warped by two separate GDCMs according to the same GDCM source feature map; finally, warped frame  $I'_t$  and warped context map  $C'_t$  are fed into PM to produce interpolation result  $\hat{I}_t$  as an approximation of  $I_t$ . Remark: for notional simplicity, we have assumed that the source frames are equally spaced in time; however, it will become clear that our framework is general enough to handle the unequal spacing case as well.

### A. Generalized Deformable Convolution Module

The input to GDCM consists of  $T + 1$  source frames  $I_0, I_1, \dots, I_T$  (or context maps  $C_0, C_1, \dots, C_T$ ) and a GDCM

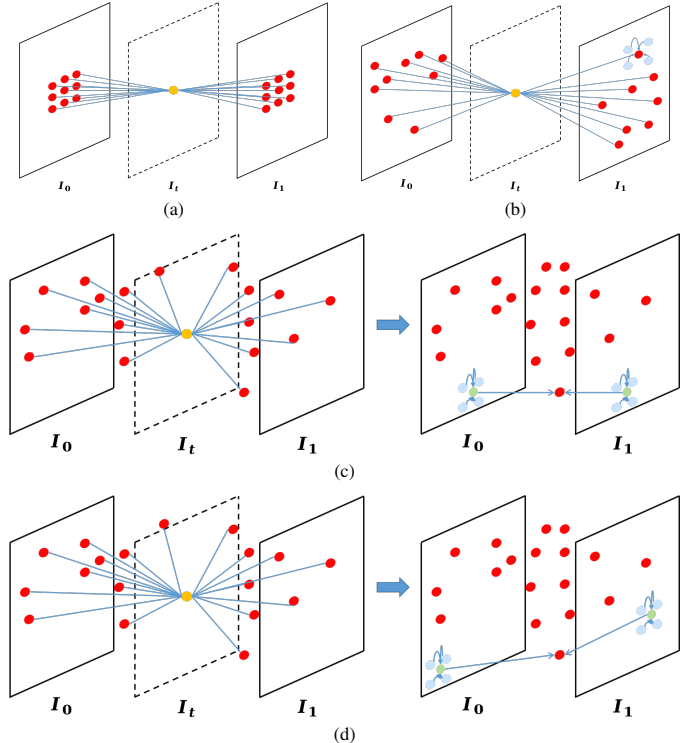


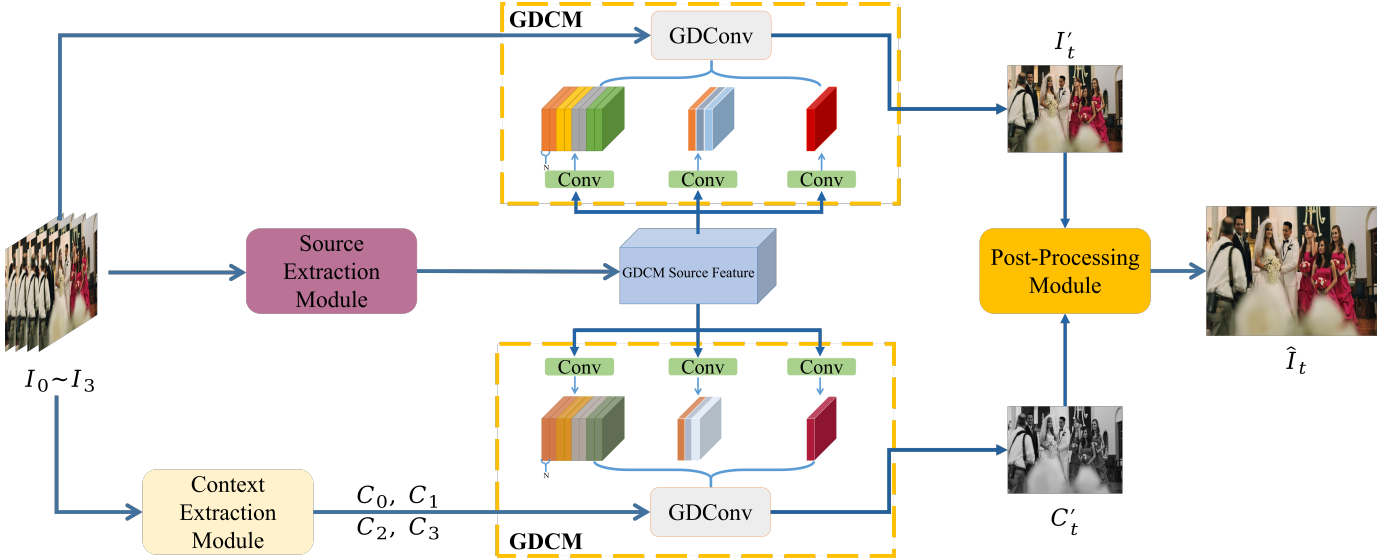
Fig. 2. Illustration of (a) conventional convolution, (b) AdaCoF, (c) basic GDConv, (d) advanced GDConv with  $T = 1$ . Here target pixels, sampling points, support points, and neighboring grid points are denoted by yellow, red, green, and blue dots, respectively. For AdaCoF, the value of each sampling point is specified via bilinear interpolation of its four neighboring grid points. For basic GDConv, the value of each sampling point is determined by its two support points via linear interpolation, or equivalently, by its eight associated grid points via trilinear interpolation. Advanced GDConv further removes the constraint that the support points need to be spatially aligned with the corresponding sampling point and allows more general interpolation methods.

source feature map. As shown in Fig. 3, three different kinds of feature maps are generated through three different convolution layers respectively and are then fed to GDConv to synthesize  $I'_t$  (or  $C'_t$ ). Since the two GDCMs are almost identical, here we only describe the upper one in detail. Moreover, as the operations on three color channels are the same, we simply regard  $I_i$  as a single-channel image. For ease of exposition, we first give a brief review of video interpolation techniques based on conventional convolution [27] and AdaCoF [19], then elaborate the improvements offered by the proposed GDConv.

Conventional convolution is employed in [27] for video frame interpolation, which can be formulated as:

$$I'_t(x, y) = \sum_{i=0}^T \sum_{m=1}^M W_m^i(x, y) \cdot I_i(x + x_m, y + y_m), \quad (1)$$

where  $W_m^i(x, y)$  is a spatially-adaptive convolution weight, and  $\{(x_m, y_m)\}_{m=1}^N$  is a collection of pre-defined convolution sampling offsets. Fig. 2 (a) provides an illustration for the special case  $T = 1$  and  $\{(x_m, y_m)\}_{m=1}^M = \{(-1, -1), (-1, 0), \dots, (1, 1)\}$  with  $M = 9$ . Ideally, the object (pixel) movement should be confined within the coverage of the convolution kernel. As such, in the presence of large motions, this approach is memory-inefficient due to the need

Fig. 3. Illustration of the architecture of GDConvNet with  $T = 3$ .

of a large number of sampling points to ensure sufficient coverage.

The inefficiency of conventional convolution is largely a consequence of pre-defined kernel shape (typically a rectangular grid). AdaCoF [19] addresses this issue by adopting spatially-adaptive deformable convolution, resulting in the following formulation:

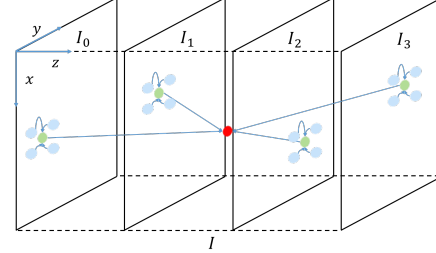
$$I'_t(x, y) = \sum_{i=0}^T \sum_{m=1}^M W_m^i(x, y) \cdot I_i(x + \Delta\alpha_m^i, y + \Delta\beta_m^i), \quad (2)$$

where  $\{(\Delta\alpha_m^i, \Delta\beta_m^i)\}_{m=1}^M$  is a collection of trainable sampling offsets. In the case where  $\Delta\alpha_m^i$  and  $\Delta\beta_m^i$  are not integers,  $I_i(x + \Delta\alpha_m^i, y + \Delta\beta_m^i)$  is specified through bilinear interpolation. Via the introduction of trainable sampling offsets, the kernel shape becomes adjustable as shown in Fig. 2 (b). For this reason, AdaCoF is able to cope with large motions using a relatively small number of sampling points. On the other hand, AdaCoF only exploits the degrees of freedom in the spatial domain. As a result, the sampling points are evenly split among the input frames. However, this is clearly suboptimal since the frames that are closer to the target intermediate frame in the temporal domain are more relevant and consequently should be allocated with more sampling points.

We shall develop a mechanism that enables flexible allocation of sampling points across the input frames. In fact, we go one step further by allowing sampling points to be freely distributed in whole space-time. The key idea is to associate each sampling point with a trainable temporal parameter  $z_n \in [0, T]$ , leading to the following formulation:

$$I'_t(x, y) = \sum_{n=1}^N W_n(x, y) \cdot I(x + \Delta x_n, y + \Delta y_n, z_n). \quad (3)$$

Here  $I$  is a function (defined on a 3D space) obtained via a judicious extension of  $I_0, I_1, \dots, I_T$  to be detailed below (see Fig. 4 for an illustration of the special case  $T = 3$ ).

Fig. 4. Construction of function  $I$  for the special case  $T = 3$  with a sampling point  $(x + \Delta x_n, y + \Delta y_n, z_n)$ , its associated support points  $(x + \Delta x_n^i, y + \Delta y_n^i, i)$ ,  $i \in \{0, 1, 2, 3\}$ , and their neighboring grid points highlighted in red, green, and blue, respectively.

Note that  $z_n$  is allowed to be any real number in  $[0, T]$  to facilitate end-to-end training. If  $z_n$  is an integer, we set  $I(x + \Delta x_n, y + \Delta y_n, z_n) = I_{z_n}(x + \Delta x_n, y + \Delta y_n)$  (following [19], [5], [44],  $I_{z_n}(x + \Delta x_n, y + \Delta y_n)$  is specified via bilinear interpolation of four neighboring grid points in the case where  $\Delta x_n$  and  $\Delta y_n$  are not integers). It can be seen that (3) reduces to (2) when  $N = (T + 1)M$  and each value in  $\{0, 1, \dots, T\}$  is taken by the same number of  $z_n$ . Now it remains to deal with non-integer valued  $z_n$  (the associated sampling point is not exactly located on an input frame). One simple solution is to set  $I(x + \Delta x_n, y + \Delta y_n, z_n)$  as  $(\lceil z_n \rceil - z_n) \cdot (I(x + \Delta x_n, y + \Delta y_n, \lceil z_n \rceil) + (z_n - \lceil z_n \rceil) \cdot I(x + \Delta x_n, y + \Delta y_n, \lceil z_n \rceil))$  (see Fig. 2 (c) for an illustration of the special case  $T = 1$ ). More generally, we attach a set of support points  $(x + \Delta x_n^i, y + \Delta y_n^i, i)$ ,  $i \in \{0, 1, \dots, T\}$ , to each sampling point  $(x + \Delta x_n, y + \Delta y_n, z_n)$ , and use their values  $I(x + \Delta x_n^i, y + \Delta y_n^i, i)$  (denoted as  $s_n^i$  for short),  $i \in \{0, 1, \dots, T\}$ , and relative positions to specify  $I(x + \Delta x_n, y + \Delta y_n, z_n)$  (denoted as  $s_n$  for short) via an interpolation function  $G$ :

$$s_n = G(\Delta x_n, \Delta y_n, z_n, \{s_n^i, \Delta x_n^i, \Delta y_n^i\}_{i=0}^T). \quad (4)$$

Illustrations of special cases  $T = 1$  and  $T = 3$  can be found in Fig. 2 (d) and Fig. 4, respectively. Note that each

support point has its own trainable spatial offset  $(\Delta x_n^i, \Delta y_n^i)$ , which is not necessarily the same as  $(\Delta x_n, \Delta y_n)$ . Moreover, there is considerable freedom in the choice of  $G$  as long as the differentiability condition needed for end-to-end training is satisfied; we will discuss several interpolation methods in Section IV-C. Finally, inspired by modulated deformable convolution [44], we rewrite (3) equivalently as:

$$I'_t(x, y) = \sum_{n=1}^N W_n \cdot I(x + \Delta x_n, y + \Delta y_n, z_n) \cdot \Delta m_n(x, y), \quad (5)$$

where  $\Delta m_n(x, y) \in [0, 1]$  is a trainable modulation term.

As illustrated in Fig. 3, three types of feature maps are generated in GDCM via three different convolution layers. The first  $2(T + 1)N$  feature maps represent spatial offsets (horizontal and vertical) for support points, and the next  $3N$  feature maps represent spatial offsets and temporal parameters for sampling points, and the last  $N$  feature maps represent modulation terms. We set the initial values of  $\Delta x_n, \Delta y_n, z_n, \Delta m_n, \Delta x_n^i$  and  $\Delta y_n^i$  as 0, 0, 0, 1, 0, and 0 respectively. The learning rate for GDCM is the same as the global learning rate.

### B. Other Modules

Now we proceed to give a brief description of the remaining modules in the proposed GDConvNet.

**Source Extraction Module:** We adopt the FPN backbone [20] to generate hierarchical features. In the bottom-up pathway, there are three levels (each consisting of two residual blocks and one convolution layer) and the associated feature maps (which are of different scales) are denoted as  $S_1, S_2$ , and  $S_3$ . The input  $P_3$  to the top level of the top-down pathway is generated from  $S_3$  through a pyramid pooling module [42];  $P_3$  is then upsampled and merged with  $S_2$  via elements-wise addition to generate  $P_2$ , which is further upsampled and merged with  $S_1$  to generate  $P_1$ . Finally,  $P_2, P_3$  are upsampled and concatenated with  $P_1$  to form the output.

**Context Extraction Module:** It is demonstrated in [26] that context information is very important for video interpolation. We use one convolution layer and two residual blocks [8] to sequentially extract contextual features. A SEblock [10] is then used to rearrange these feature maps, and finally its output is smoothed by a convolution layer.

**Post-Processing Module:** To refine the warped image, we adopt the GridDehazeNet architecture [21], where each row is associated with a different scale and contains five RDB blocks [41] while each column can be considered as a bridge connecting different scales through downsampling or upsampling modules, which decrease or increase the size of feature maps by a factor of two. Instead of employing the hard attention mechanism in [21], we use SEBlocks [10] to adaptively rebalance the incoming information flows at junctions of GridDehazeNet.

## III. UNDERSTANDING GENERALIZED DEFORMABLE CONVOLUTION IN VIDEO INTERPOLATION

In this section, we shall place generalized deformable convolution in a general context and explain why it is an effective

mechanism for video interpolation.

### A. Related Works

Generalized deformable convolution is conceptually related to several existing ideas in the literature.

**Deformable Convolution:** There are abundant works on variants of conventional convolution with improved performance, including active convolution [13], dynamic filter [14], atrous convolution [9], among others. A culminating achievement of this line of research is deformable convolution [5], [44]. Our generalized deformable convolution degenerates to conventional deformable convolution [5], [44] if the temporal dimension is not present, and its basic form shown in Fig. 2 (c) can be viewed as a 3D-version of deformable convolution.

**Non-Local Network:** In deep learning, non-locality means that the receptive field is not restricted to a certain local region and can capture long-range context information. The receptive field of conventional convolution is typically a fixed grid and consequently is local in nature. Significant efforts have been devoted to addressing this issue [43], [42], [9], [37]. Arguably the most successful one is [37], which takes all possible spatial positions into consideration; however, this comes at the cost of high memory usage. In contrast, generalized deformable convolution is memory-efficient as it is able to achieve non-local coverage and capture long-range context information with a relatively small kernel by adaptively and intelligently selecting sampling points in space-time.

**Attention Mechanism:** Attention mechanism enables differentiated treatment of different input features according to their relevant importance, which has shown to yield significant performance gain in many vision tasks. Traditionally, it can be divided into spatial-wise attention [36] and channel-wise/temporal-wise attention [10]. Recently, there are also attempts [29], [38] to combine these two types of attention; nevertheless, in these approaches spatial-wise and channel-wise/temporal-wise attention maps are still first generated separately. It is interesting to note that generalized deformable convolution offers a natural way to consolidate these two types of attention by suitably modulating sampling points at different locations in space-time.

**Non-Linearity:** The conventional approach to increasing the non-linearity of convolutional neural networks [18], [32], [17] is by stacking more non-linear modules [17], [7]. However, it has been recognized that a more effective approach is to allow the functionalities of constituent modules to be input-dependent [10], [12], [36]. From this perspective, generalized deformable convolution manages to convert a linear convolution operation to a highly non-linear operation by adaptively adjusting its kernel according to the input, yielding enhanced learning capabilities.

### B. Comparison with State-of-the-Art Video Interpolation Algorithms

The state-of-the-art video interpolation methods can be divided into two categories: flow-based methods and kernel-based methods. For illustrative purposes, we shall consider the

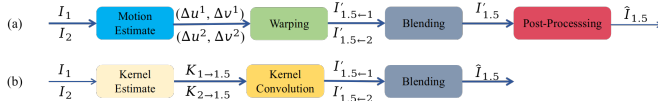


Fig. 5. Illustration of (a) flow-based video interpolation pipeline and (b) kernel-based video interpolation pipeline.

simple scenario where two source frames  $I_1$  and  $I_2$  are used to predict one target frame  $I_{1.5}$  unless specified otherwise.

**Flow-based:** These methods admit a common mathematical formulation as follows:

$$I'_{1.5 \leftarrow 1}(x, y) = I_1(x + \Delta u^1, y + \Delta v^1), \quad (6)$$

or

$$I'_{1.5 \leftarrow 2}(x, y) = I_2(x + \Delta u^2, y + \Delta v^2), \quad (7)$$

where  $(\Delta u^1, \Delta v^1)$  and  $(\Delta u^2, \Delta v^2)$  are respectively optical flow fields from  $I_{1.5}$  to  $I_1$  and  $I_2$  while  $I'_{1.5 \leftarrow 1}$  and  $I'_{1.5 \leftarrow 2}$  denote two warped images from two directions. The pipeline of flow-based methods is illustrated in Fig. 5 (a). First two input frames are used to estimate optical flow maps, typically with the help of optical flow estimation network [30], [6], [11], [35] or U-Net [31]; the input frames are then warped according to these optical flow maps; finally, blending and post-processing operations are performed to generate the final output. The linear motion model is widely adopted in flow map estimation. However, this model is not accurate for describing accelerated and curvilinear motions. To handle such complex motions, a quadratic model is proposed in [39], where  $(\Delta u^1, \Delta v^1)$  and  $(\Delta u^2, \Delta v^2)$  are estimated based on four frames  $I_0$ ,  $I_1$ ,  $I_2$ , and  $I_3$  instead of just  $I_1$  and  $I_2$ . To understand the connection with our method, it is instructive to consider a special case of (5) with  $N = 1$ , where  $z_1 = 1$ ,  $(\Delta x_1, \Delta y_1) = (\Delta x_1^1, \Delta y_1^1)$ , or  $z_1 = 2$ ,  $(\Delta x_1, \Delta y_1) = (\Delta x_1^2, \Delta y_1^2)$ :

$$\begin{aligned} I'_{1.5 \leftarrow 1}(x, y) &= W_1 \cdot I(x + \Delta x_1, y + \Delta y_1, 1) \cdot \Delta m_1 \\ &= W_1 \cdot I_1(x + \Delta x_1^1, y + \Delta y_1^1) \cdot \Delta m_1, \end{aligned} \quad (8)$$

or

$$\begin{aligned} I'_{1.5 \leftarrow 2}(x, y) &= W_1 \cdot I(x + \Delta x_1, y + \Delta y_1, 2) \cdot \Delta m_1 \\ &= W_1 \cdot I_2(x + \Delta x_1^2, y + \Delta y_1^2) \cdot \Delta m_1. \end{aligned} \quad (9)$$

One can readily recover (6) and (7) from (8) and (9) by setting  $W_1 = \Delta m_1 = 1$  and interpreting  $(\Delta x_1^i, \Delta y_1^i)$  as  $(\Delta u^i, \Delta v^i)$ ,  $i = 1, 2$ . Similarly to the case with  $(\Delta u^1, \Delta v^1)$  and  $(\Delta u^2, \Delta v^2)$  in [39], the estimation of offsets  $(\Delta x_1^1, \Delta y_1^1)$  and  $(\Delta x_1^2, \Delta y_1^2)$  can also benefit from more than two source frames. More importantly, in our method, the offset estimation does not rely on any prescribed mathematical model and is carried out in a purely data-driven manner; as such, it can cope with real-world motions more flexibly and accurately. Furthermore, for the general version of our method, the number of sampling points can be set greater than 1 (i.e.,  $N > 1$ ), which, together with the freedom in choosing the space-time coordinates of sampling points and the relaxation of the constraint  $(\Delta x_n, \Delta y_n) = (\Delta x_n^i, \Delta y_n^i)$ , makes it possible to capture complex diffusion and dispersion effects. Finally, we would like to point out that the space-time interpolation

operation in our method plays a role similar to that of the blending operation in some existing flow-based methods [3], [15], [40] (see also Fig. 5 (a)), but requires fewer parameters as it is performed at the sampling point level.

**Kernel-based:** These methods [27], [28], [18] generate two sets of spatially-adaptive convolution kernels and use them to convolve with source frame patches to get the predicted target frames  $I'_{1.5 \leftarrow 1}$ ,  $I'_{1.5 \leftarrow 2}$  from two sides, which are then blended at the pixel level to get final interpolation result:

$$\begin{aligned} \hat{I}_{1.5}(x, y) &= I'_{1.5 \leftarrow 1}(x, y) + I'_{1.5 \leftarrow 2}(x, y) \\ &= K_1(x, y) * I_1(x, y) + K_2(x, y) * I_2(x, y). \end{aligned} \quad (10)$$

The pipeline of kernel-based methods is shown in Fig. 5 (b). Note that in the presence of complex motions, [27], [28] need to adopt large kernels to ensure sufficient coverage, which is inflexible and memory-inefficient. AdaCoF [19] addresses this issue by adopting deformable convolution. Nevertheless, sampling points in AdaCoF are only spatially adaptive. In contrast, the proposed method can make more effective use of sampling points by freely exploring in space-time (not just in the spatial domain). As such, it often suffices to employ small kernels even when dealing with very complex motions. Our method also has the additional advantage of blending images at the sampling point level (in the form of space-time interpolation), which is more efficient than blending at the pixel level in kernel-based methods.

#### IV. FOUR-FRAME INTERPOLATION EXPERIMENTS

Due to its flexibility, our method can leverage arbitrary number of frames for interpolation. Here we focus on the four-frame interpolation case. The experimental results for two-frame interpolation will be presented in Section V.

##### A. Implementation Details

We use four source frames  $I_0$ ,  $I_1$ ,  $I_2$ , and  $I_3$  to synthesize the target frame  $I_{1.5}$ . In GDConv, the number of sampling points for each warped pixel is set to 25. The loss function, the training dataset, and the training strategy are described below.

**Loss Function:** We optimize our network with respect to the following loss function:

$$\begin{aligned} \mathcal{L} &= \mathcal{L}_w + \lambda \mathcal{L}_r \\ &= \sum_x \rho(I'_t(x) - I_{GT}(x)) + \lambda \sum_x \rho(\hat{I}_t(x) - I_{GT}(x)), \end{aligned} \quad (11)$$

where  $\rho(x) = \sqrt{x^2 + \epsilon^2}$  is the Charbonnier penalty function [4],  $I_{GT}$  is the ground-truth frame, and  $\lambda$  is a hyper-parameter to balance the warped loss  $\mathcal{L}_w$  and the refined loss  $\mathcal{L}_r$ . We set  $\epsilon = 10^{-6}$  and  $\lambda = 0.5$ .

**Training DataSet:** The Vimeo90k Septuplet training dataset [40] is used to train our model. This training dataset is composed of 64612 seven-frame sequences with resolution  $256 \times 448$ . We use the first, the third, the fifth, and the seventh frames (corresponding to  $I_0$ ,  $I_1$ ,  $I_2$ , and  $I_3$ , respectively) of each sequence to predict the fourth one (corresponding to  $I_{1.5}$ ). We randomly crop image patches of size  $256 \times 256$  for training.

TABLE I  
MEAN OF THE SQUARED DISTANCE.

$(d_x)^2$	$(d_y)^2$	$(d_z)^2$
0.0025	0.0010	0.2009

Horizontal/vertical flipping as well as temporal order reversal is performed for data augmentation.

**Training Strategy:** Different from [2], [3], [40], our network can be trained from scratch without relying on any pre-trained model. We adopt Adam optimizer [16] with a batch size of 8, where  $\beta_1$  and  $\beta_2$  are set as the default values 0.9 and 0.999, respectively. We train our network for 14 epochs in total with the initial learning rate set as  $10^{-3}$ , and the learning rate is reduced by a factor of two every 4 epochs for the first 8 epochs and by a factor of five every 2 epochs for the last 6 epochs. The training is carried out on four 1080Ti GPUs.

### B. Evaluation Datasets

The following three datasets are used for performance evaluation.

**Vimeo90K Septuplet Test Set [40]:** This dataset consists of 7824 video sequences, each with 7 frames. As in the case of Vimeo90K Septuplet training dataset, the first, the third, the fifth, and the seventh frames of each sequence are leveraged to synthesize the fourth one. The image resolution of this dataset is  $256 \times 448$ .

**Gopro Dataset [25]:** This dataset contains 33 high-resolution videos recorded by hand-held camera. The frame rate of each video is  $240\text{fps}$ , and the image resolution is  $720 \times 1280$ . The dataset is released in image format with a total of 35782 images. We successively group every 25 consecutive images as a test sequence, and resize the images to  $360 \times 480$ . Finally, 1392 test sequences are selected; for each sequence, the first, the ninth, the seventeenth, and the twenty-fifth frames (corresponding to  $I_0$ ,  $I_1$ ,  $I_2$ , and  $I_3$ , respectively) are used to synthesize the thirteenth frame (corresponding to  $I_{1.5}$ ).

**Adobe240 Dataset [34]:** This dataset consists of 133  $240\text{fps}$  videos in total, where the resolution of each video is  $720 \times 1280$ . These videos are also recorded by hand-held camera, and mainly contain outdoor scenes. Different from Gopro dataset, this dataset is released in video format. We extract 7479 non-overlapped test sequences, each with 25 frames.

### C. Interpolation Methods

Many existing interpolation methods can be leveraged to generate sampling points  $s_n = I(x + \Delta x_n, y + \Delta y_n, z_n)$  in accordance with their positions and the corresponding support points  $s_n^i = I(x + \Delta x_n^i, y + \Delta y_n^i, i)$ ,  $i \in \{0, 1, \dots, T\}$  only if the function satisfies the derivable condition as aforementioned. We study the effect of different interpolation methods to the performance of video interpolation, including the Trilinear interpolation, the 3-axis and 1-axis inverse distance, and the polynomial interpolation.

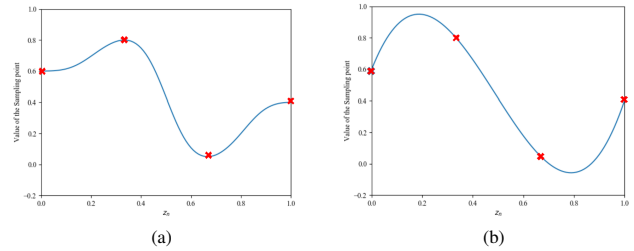


Fig. 6. Illustration of (a) inverse distance weighted interpolation (1D version) and (b) polynomial interpolation with support points highlighted in red. Here  $s_n^0 = 0.6$ ,  $s_n^1 = 0.8$ ,  $s_n^2 = 0.05$ , and  $s_n^3 = 0.4$ , respectively.

**1) Linear Interpolation:** This is one of the simplest interpolation methods. It can be formulated as:

$$s_n = \sum_{i=0}^T \max(0, 1 - |z_n - i|) \cdot s_n^i. \quad (12)$$

Note that even if  $T > 1$ , only two adjacent support points are taken into consideration in (12) for interpolating  $s_n$  (the maximum operation suppresses the contribution of other support points). We regard this interpolation method as the baseline in comparisons.

**2) Inverse Distance Weighted Interpolation (3D version):** In contrast to linear interpolation, this method makes use of all support points (see Fig. 4) as follows:

$$s_n = \frac{\sum_{i=0}^T w_i \cdot s_n^i}{\sum_{i=0}^T w_i}, \quad (13)$$

where  $w_i = 1/((d_x^i)^2 + (d_y^i)^2 + (d_z^i)^2)$ ,  $d_x^i = |\Delta x_n - \Delta x_n^i|/H$ ,  $d_y^i = |\Delta y_n - \Delta y_n^i|/W$ , and  $d_z^i = |z_n - i|/T$ . The quantitative comparisons in Table II indicate that leveraging all support points instead of just two adjacent points yields better performance. Table I shows the means of  $(d_x^i)^2$ ,  $(d_y^i)^2$ , and  $(d_z^i)^2$  (averaged over  $i$ ), denoted as  $(d_x)^2$ ,  $(d_y)^2$  and  $(d_z)^2$ , respectively. It is clear that  $(d_x)^2$  and  $(d_y)^2$  are about two orders of magnitude smaller than  $(d_z)^2$ . This implies that it might suffice to set the weights based on the temporal information alone, which naturally suggests the following interpolation method.

**3) Inverse Distance Weighted Interpolation (1D version):** Setting  $w_i = 1/(d_z^i)^2$  in (13) leads to the 1D version of inverse distance weighted interpolation (see Fig. 6 (a) for an example with  $T = 3$ ). The quantitative results of this interpolation method are shown in Table II. Somewhat surprisingly, the 1D version slightly outperforms its 3D counterpart. One possible reason is that focusing on the dominant dimension enables more effective use of the training data and consequently yields more accurate interpolation results. This suggests that it might be possible to further improve the performance by employing more advanced 1D interpolation methods.

**4) Polynomial Interpolation:** This method uses a polynomial function of degree  $T$  to perform interpolation. More specifically, we have:

$$G = a_0 + a_1 z_n + \dots + a_T z_n^T, z \in [0, T], \quad (14)$$

TABLE II

QUANTITATIVE COMPARISONS ON VIMEO90K SEPTULET TEST SET, GOPRO DATASET AND ADOBE240 DATASET, WHERE THE FIRST PLACE AND THE SECOND PLACE ARE HIGHLIGHTED IN RED AND BLUE, RESPECTIVELY.

Method	#Parameters (million)	Vimeo90K		Gopro		Adobe240	
		PSNR	SSIM	PSNR	SSIM	PSNR	SSIM
Ours-Poly	5.1	<b>35.58</b>	<b>0.9580</b>	<b>30.49</b>	<b>0.9180</b>	<b>34.53</b>	<b>0.9456</b>
Ours-1 Inverse	5.1	35.08	0.9541	30.16	0.9099	<b>34.36</b>	<b>0.9436</b>
Ours-3 Inverse	5.1	35.01	0.9535	30.12	0.9099	34.27	0.9427
Ours-Linear	5.1	34.96	0.9534	30.06	0.9092	34.20	0.9422
AdaCoF	21.8	33.92	0.9453	28.45	0.8734	33.17	0.9305
QVI	29.2	<b>35.19</b>	<b>0.9563</b>	<b>30.24</b>	<b>0.9230</b>	33.06	0.9393
Slomo	39.6	33.73	0.9453	28.50	0.8827	31.94	0.9264
SepConv	21.6	33.65	0.9435	28.66	0.8798	33.41	0.9349
DVF	3.8	30.79	0.8912	25.13	0.7633	22.33	0.6159
Phase	-	30.52	0.8854	26.17	0.8135	31.20	0.8930

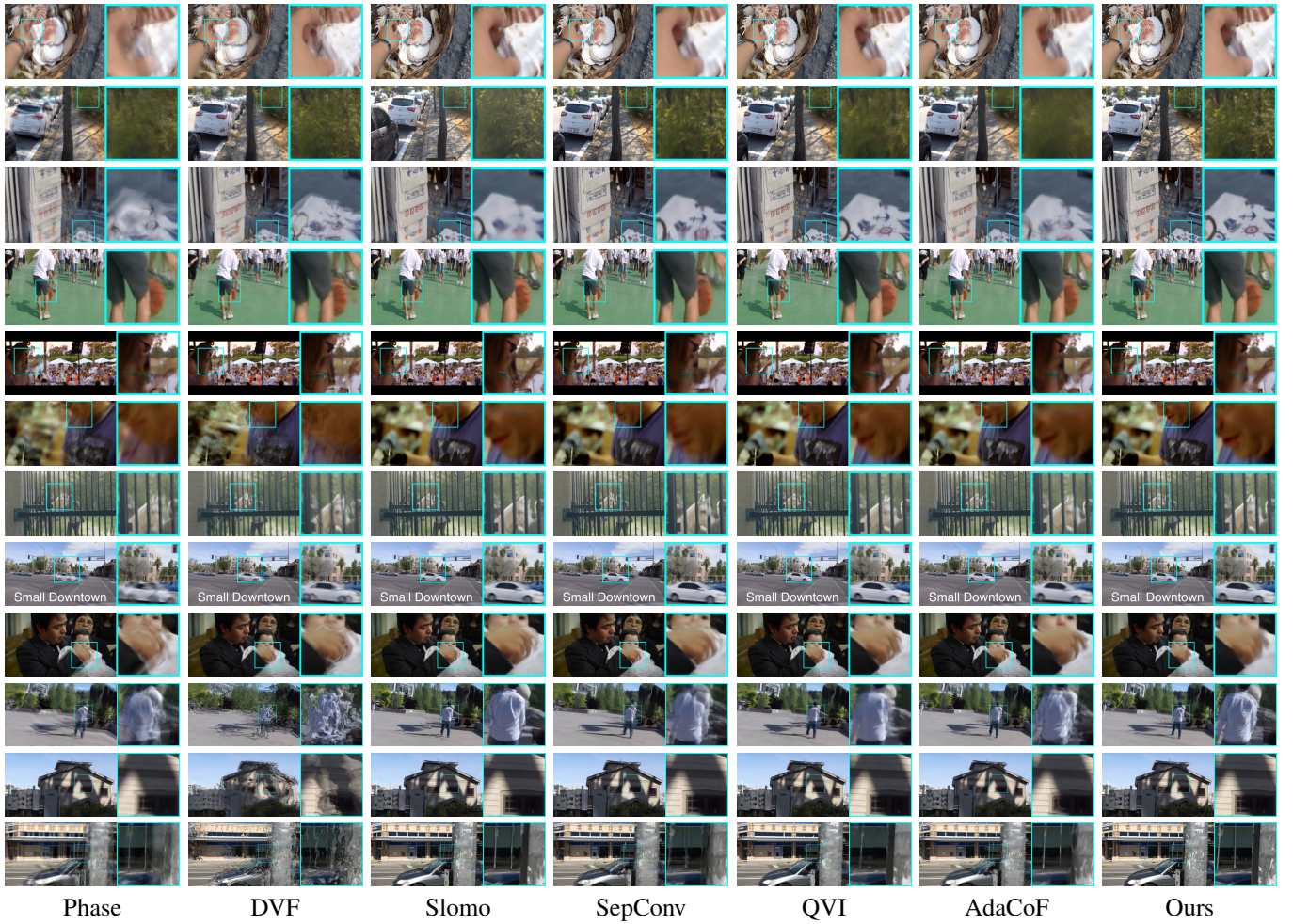


Fig. 7. Qualitative comparisons of different video interpolation algorithms.

where the coefficients  $a_0, a_1, \dots$ , and  $a_T$  can be uniquely determined by jointly solving  $T+1$  linear equations  $G|_{z_n=i} = s_n^i$ ,  $i \in \{0, 1, \dots, T\}$ . Fig. 6 (b) provides an example of polynomial interpolation with  $T = 3$ . In contrast to inverse distance weighted interpolation (1D version), polynomial interpolation is able to generate values beyond upper and lower limits of  $s_n^i$ ,  $i \in \{0, 1, \dots, T\}$ . This extra freedom might be the reason why the latter leads to 0.5 dB improvement over

the former as shown in Table. II.

It should be emphasized that sampling points and their associated support points are still selected in 3D space-time even if a 1D interpolation method is adopted; as such, the overall method is intrinsically 3D.

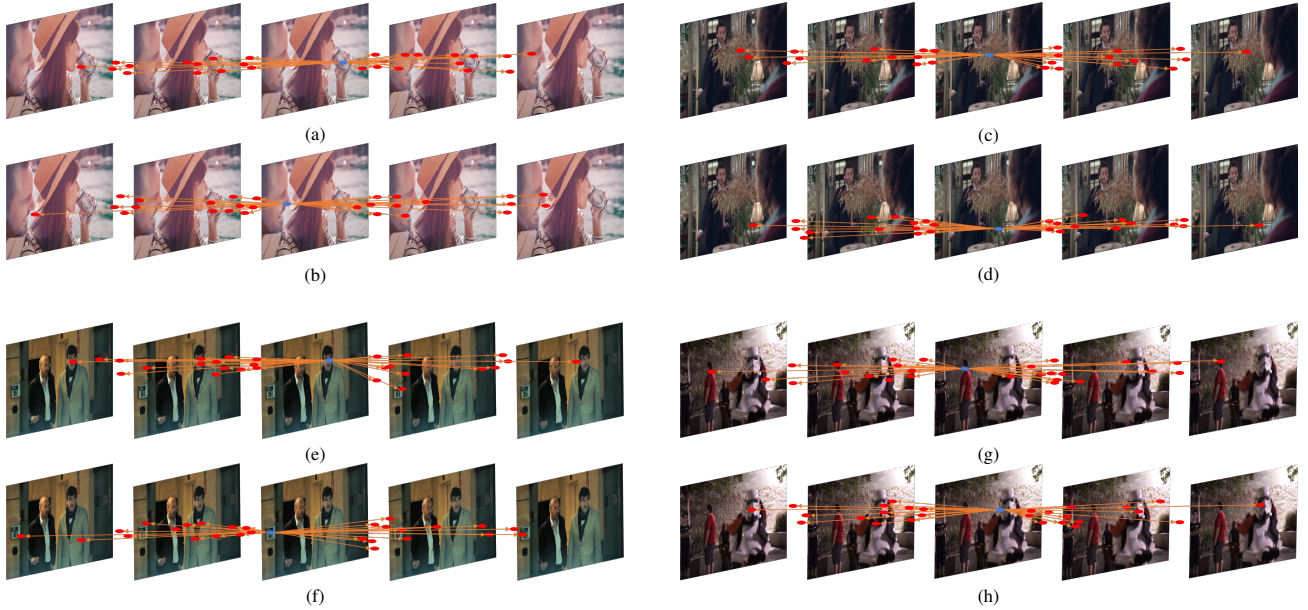


Fig. 8. Visualization of sampling points in GDCM when  $t = 1.5$ . Here ((a), (b)), ((c), (d)), ((e), (f)), and ((g), (h)) illustrate two different pixels in a same target intermediate frame and their associated sampling points respectively. It can be seen that sampling points are not exclusively located between  $I_1$  and  $I_2$ ; indeed, there are some between  $I_1$  and  $I_2$ , and between  $I_2$  and  $I_3$ . This indicates that the information from  $I_1$  and  $I_2$  is more significant for synthesizing  $I_t$ , but  $I_0$  and  $I_3$  also contribute to the synthesized result.

#### D. Comparison with the State-of-the-Art

We compare our GDConvNet with the state-of-the-art video interpolation algorithms on the aforementioned three evaluation datasets. Specifically, the following ones are chosen for comparison: the phase-based method (Phase) [24], separable adaptive convolution (SepConv) [28], deep voxel flow (DVF) [11], SuperSlomo (Slomo) [15], quadratic video interpolation (QVI) [39], and adaptive collaboration of flows (AdaCoF) [19]. The experimental results show that our method performs favorably against the ones under consideration. For fair comparison, DVF, Slomo, QVI, and AdaCoF are retrained on our training dataset; as the SepConv training code is not available, we choose to directly evaluate the original SepConv model.

In Table II, we quantitatively compare our method with the state-of-the-art on the evaluation datasets under two well-known objective image quality metrics, PSNR and SSIM. It can be seen that the proposed method ranks consistently at the top (except for the Gopro dataset on which our method comes in a close second in terms of SSIM value). Overall, our method has a clear advantage under joint consideration of cost and performance; in particular, while QVI also shows very competitive performance, its model size is about 6 times of ours.

Fig. 7 shows the qualitative comparisons. It can be seen that our method produces clearer and sharper results. For example, ours is capable of generating smooth edges around the hand compared with that of Phase, DVF, SepConv, Slomo, QVI, and AdaCoF.

#### E. Ablation Study

In our ablation studies, we adopt polynomial interpolation and consider a simplified version of GDConvNet with CEM and the associated GDCM as well as PM removed. This

simplification greatly reduces the training time, and more importantly, enables us to focus on the most essential aspects of GDConvNet.

1) *Generalized Deformable Convolution Module*: In order to validate the effectiveness of our design, we compare the proposed GDConv with DConv (more precisely, spatially-adaptive DConv or modulated DConv) adopted by [19] as well as several variants of GDConv.

TABLE III  
COMPARISONS OF DCONV, GDCONV WITH DIFFERENT NUMBERS OF SAMPLING POINTS, AND SOME VARIANTS OF GDCONV.

Method	# Sampling Points	PSNR	SSIM
GDConv	36	32.82	0.9236
	1	33.40	0.9342
	9	33.98	0.9414
	25	<b>34.20</b>	<b>0.9436</b>
	36	34.17	0.9430
Variant (a)	25	32.99	0.9274
Variant (b)	25	33.24	0.9310
Variant (c)	25	33.92	0.9410
Variant (d)	25	<b>34.20</b>	<b>0.9436</b>

**Superiority of GDConv over DConv**: As mentioned earlier, the proposed GDConv is able to exploit the given source frames in accordance with their relevance to the target intermediate frame in terms of temporal distance. In contrast, the performance of DConv is limited by the inflexibility in choosing the number of sampling points from each source frame. For instance, consider the case where 4 consecutive frames are used for interpolation and the convolution kernel size is set to 3. DConv is constrained to select 9 sampling points from each frame. This is inefficient from the perspec-

tive of resource allocation since the source frames closer to the target intermediate frame in time are conceivably more informative and should receive more attention. In this sense, the proposed GDConv is more desirable as it is endowed with complete freedom to select sampling points in space-time. Specifically, in GDConv, the number of sampling points in each frame is adjustable according to the significance of that frame in synthesis; more importantly, sampling points are not even required to lie exactly on the source frames, and are allowed to be anywhere in the spatio-temporal domain specified by their associated parameters  $\Delta x_n$ ,  $\Delta y_n$  and  $z_n$  (see Fig. 8 for some visualization results). This mechanism is especially important for video interpolation since it is better suited to cope with complex and irregular inter-frame motions. In Table III, we provide quantitative comparisons of DConv and GDConv. Here the number of input source frames is 4. In GDConv, the number of sampling points is set to 36. For fair comparison, the kernel size in DConv is chosen to be 3; thus, there are  $3 \times 3 \times 4 = 36$  sampling points in total as well. It is evident that the proposed GDConv achieves better performance in terms of PSNR and SSIM metrics.

**Importance of Spatio-Temporal Freedom:** We consider the following 4 variants of GDConv to illustrate the importance of spatio-temporal freedom for sampling points.

- (a) No spatio-temporal freedom:  $(\Delta x_n^i, \Delta y_n^i)$ ,  $i \in \{0, 1, 2, 3\}$ , are identical and fixed to be a distinct point in a  $5 \times 5$  grid  $\{(-2, -2), (-2, -1), \dots, (2, 2)\}$ , and  $z_n = 1.5$ .
- (b) Limited spatial freedom, no temporal freedom:  $(\Delta x_n^i, \Delta y_n^i)$ ,  $i \in \{0, 1, 2, 3\}$ , are identical but trainable, and  $z_n = 1.5$ .
- (c) Limited spatial freedom, complete temporal freedom:  $(\Delta x_n^i, \Delta y_n^i)$ ,  $i \in \{0, 1, 2, 3\}$ , are identical but trainable, and  $z_n$  is trainable.
- (d) Complete spatio-temporal freedom:  $(\Delta x_n^i, \Delta y_n^i)$ ,  $i \in \{0, 1, 2, 3\}$ , can be different from each other and are individually trainable, and  $z_n$  is also trainable.

The experiment results are shown in Table III. One can easily find that the performance rises progressively with the availability of every additional freedom. It is worth noting that temporal parameter  $z_n$  is better interpreted as effective time instead of physical time. Indeed, forcing  $z_n = 1.5$  limits the degrees of freedom and jeopardizes the performance.

**Choice of the Number of Sampling Points:** We further investigate how to choose the number of sampling points in GDConv. As shown in Table III, with the increase in the number of sampling points, the performance improves initially but becomes saturated eventually. In particular, using more than 36 sampling points cannot further enhance the quality of synthesized frames.

TABLE IV  
COMPARISONS FOR DIFFERENT NUMBERS OF REFERENCE FRAMES.

Reference Frames	PSNR	SSIM
$I_1, I_2$	33.69	0.9416
$I_0, I_1, I_2$	33.97	0.9427
$I_0, I_1, I_2, I_3$	<b>34.20</b>	<b>0.9436</b>

TABLE V  
COMPARISONS FOR DIFFERENT NUMBERS OF GENERATION FRAMES.

Reference Frames	PSNR	SSIM
$I_1, I_2$	33.69	0.9416
$I_0, I_1, I_2$	33.84	0.9418
$I_0, I_1, I_2, I_3$	<b>34.05</b>	<b>0.9434</b>

2) *Input Length and Offset Generation:* So far we have assumed that all 4 source frames  $I_0$ ,  $I_1$ ,  $I_2$ , and  $I_3$  participate in generating offsets (as well as  $z_n$  and  $\Delta m_n$ ) and predicting the target intermediate frame  $I_{1.5}$ . It is interesting to study how the proposed method performs if one only utilizes a subset of source frames. In fact, our framework is flexible enough to allow using different subsets of source frames for offset generation and frame prediction separately. For clarity, we shall refer to source frames used for generating offsets as generation frames and those directly involved in predicting the target intermediate frame as reference frames; for example, if we use  $I_0$ ,  $I_1$ ,  $I_2$  to generate offsets for  $I_1$  and  $I_2$ , which are subsequently leveraged to predict  $I_{1.5}$ , then  $I_0$ ,  $I_1$ ,  $I_2$  are generation frames while the latter two are reference frames. We first study the scenario with the same subset of source frames used for both purposes. It is clear from Table IV that the interpolation result improves progressively with the increase in the number of reference frames (as well as generation frames). We further investigate the scenario where reference frames and generation references are not necessarily the same. Specifically, we fix  $I_1$ ,  $I_2$  to be reference frames, and consider various combinations of generation frames. It can be seen from Table V that increasing the number of generation frames leads to better performance. This is consistent with a similar finding regarding flow-based methods: namely, it is profitable to have three or more generation frames as that opens the door for exploiting higher-order approximation of motion trajectories (instead of relying on linear approximation, which is basically the only available choice in the case with just two generation frames). Finally, comparing the corresponding rows in Table IV and Table V reveals that the interpolation result can also benefit from the increase in the number of reference frames (when generation frames are fixed).

## V. TWO-FRAMES INTERPOLATION EXPERIMENTS

As described earlier, our method is able to handle arbitrary number of frames. To substantiate this claim, here we conduct two-frame interpolation experiments (i.e., using  $I_0$  and  $I_1$  to predict  $I_{0.5}$ ).

### A. Implementation Details

We adopt polynomial interpolation and set the number of sampling points for each warped pixel to 25 in GDConv. The training dataset and the training strategy are described below.

**Training Dataset:** The Vimeo90k interpolation training dataset [40] is used to train our model. This training dataset is composed of 51312 triplets with resolution  $256 \times 448$ . We use the first frame and the third frame (corresponding to  $I_0$  and  $I_1$ , respectively) of each triplet to predict the second one

TABLE VI

QUANTITATIVE COMPARISONS ON VIMEO90K INTERPOLATION TEST SET, UCF101 DATASET AND MIDDLEBURY-OTHER DATASET, WHERE THE FIRST PLACE AND THE SECOND PLACE ARE HIGHLIGHTED IN RED AND BLUE, RESPECTIVELY.

Method	#Parameters (million)	UCF101		Vimeo90K		Middlebury
		PSNR	SSIM	PSNR	SSIM	IE
MIND	7.60	33.93	0.9661	33.50	0.9429	3.35
DVF	3.80	34.12	0.9631	31.54	0.9462	7.75
ToFlow	1.07	34.58	0.9667	33.73	0.9682	2.51
SepConv-Lf	21.6	34.69	0.9655	33.45	0.9674	2.44
SepConv-L1	21.6	34.78	0.9669	33.79	0.9702	2.27
MEMC-Net	70.3	34.96	0.9682	34.29	0.9739	2.12
DAIN	24.0	<b>34.99</b>	<b>0.9683</b>	<b>34.71</b>	<b>0.9756</b>	<b>2.04</b>
AdaCoF	21.8	<b>34.99</b>	0.9682	33.43	0.9677	2.43
Ours	5.6	<b>35.16</b>	<b>0.9683</b>	<b>34.99</b>	<b>0.9750</b>	<b>2.03</b>

(corresponding to  $I_{0.5}$ ). We randomly crop image patches of size  $256 \times 256$  for training. Horizontal/vertical flipping, as well as temporal order reversal, is performed for data augmentation.

**Training Strategy:** It is the same as the four-frame case except that we train our network for 20 epochs in total. The initial learning remains to be  $10^{-3}$ ; the learning rate is reduced by a factor of two every 4 epochs for the first 12 epochs and by a factor of five every 4 epochs for the last 8 epochs.

### B. Evaluation Datasets

Following [2], we evaluate the proposed GDConvNet on three public datasets (Vimeo90k Interpolation Test Set [40], UCF101 Test Dataset[33], and Middlebury-Other Dataset [1] and compare it with the state-of-the-art.

**Vimeo90k Interpolation Test Set [40]:** This dataset consists of 3782 video sequences, each with 3 frames. As in the case of Vimeo90K interpolation training dataset, the first frame and the third frame of each sequence are leveraged to synthesize the second one. The image resolution of this dataset is  $256 \times 448$ .

**UCF101 Test Dataset[33]:** The UCF101 dataset contains 379 triplets with a large variety of human actions. The image resolution of this dataset is  $256 \times 256$ .

**Middlebury-Other Dataset [1]:** The Middlebury-Other dataset is another commonly used benchmark for video interpolation, which contains 12 triplets in total. Most of the images in this dataset are of resolution  $640 \times 480$ . Again, we use the first frame and the third frame to predict the second one.

### C. Experimental Results

We compare our GDConvNet with the state-of-the-art video interpolation algorithms on the aforementioned datasets. Specifically, the following ones are chosen for comparison: MIND [23], DVF [11], SepConv [28], CtxSyn [26], ToFlow [40], SuperSlomo [15], MEMC-Net [3], DAIN [2], and AdaCoF [19].

In Table VI, we quantitatively compare our method with the state-of-the-art on Vimeo90k and UCF101 under PSNR and SSIM while interpolation Error [32] (IE) is used as a

performance measure for the Middlebury-Other dataset. It can be seen that the proposed method performs favorably against those under consideration. Overall, our method has a clear advantage under joint consideration of cost and performance. In particular, although DAIN [2] also shows very competitive performance, its model size is about 5 times of ours. In addition, our method can be trained from scratch while DAIN [2] needs to rely on a pre-trained model.

## VI. CONCLUSION

In this paper, a new mechanism named generalized deformable convolution is proposed to tackle the video interpolation problem. This mechanism unifies the essential ideas underlying flow-based and kernel-based methods and resolves some performance-limiting issues. It should be noted that the proposed mechanism is largely generic in nature, and is potentially applicable to a wide range of problems, especially those involving video data (e.g., video super-resolution, enhancement, and quality mapping). Exploring such applications is an endeavor well worth undertaking.

## REFERENCES

- [1] Baker, S., Scharstein, D., Lewis, J., Roth, S., Black, M.J., Szeliski, R.: A database and evaluation methodology for optical flow. *International journal of computer vision* **92**(1), 1–31 (2011)
- [2] Bao, W., Lai, W.S., Ma, C., Zhang, X., Gao, Z., Yang, M.H.: Depth-aware video frame interpolation. In: *Proceedings of the IEEE Conference on Computer Vision and Pattern Recognition*. pp. 3703–3712 (2019)
- [3] Bao, W., Lai, W.S., Zhang, X., Gao, Z., Yang, M.H.: Memc-net: Motion estimation and motion compensation driven neural network for video interpolation and enhancement. *IEEE transactions on pattern analysis and machine intelligence* (2019)
- [4] Charbonnier, P., Blanc-Feraud, L., Aubert, G., Barlaud, M.: Two deterministic half-quadratic regularization algorithms for computed imaging. In: *Proceedings of 1st International Conference on Image Processing*. vol. 2, pp. 168–172. IEEE (1994)
- [5] Dai, J., Qi, H., Xiong, Y., Li, Y., Zhang, G., Hu, H., Wei, Y.: Deformable convolutional networks. In: *Proceedings of the IEEE international conference on computer vision*. pp. 764–773 (2017)
- [6] Dosovitskiy, A., Fischer, P., Ilg, E., Hausser, P., Hazirbas, C., Golkov, V., Van Der Smagt, P., Cremers, D., Brox, T.: Flownet: Learning optical flow with convolutional networks. In: *Proceedings of the IEEE international conference on computer vision*. pp. 2758–2766 (2015)
- [7] He, K., Zhang, X., Ren, S., Sun, J.: Delving deep into rectifiers: Surpassing human-level performance on imagenet classification. In: *Proceedings of the IEEE international conference on computer vision*. pp. 1026–1034 (2015)

- [8] He, K., Zhang, X., Ren, S., Sun, J.: Deep residual learning for image recognition. In: Proceedings of the IEEE conference on computer vision and pattern recognition. pp. 770–778 (2016)
- [9] Holschneider, M., Kronland-Martinet, R., Morlet, J., Tchamitchian, P.: A real-time algorithm for signal analysis with the help of the wavelet transform. In: Wavelets, pp. 286–297. Springer (1990)
- [10] Hu, J., Shen, L., Sun, G.: Squeeze-and-excitation networks. In: Proceedings of the IEEE conference on computer vision and pattern recognition. pp. 7132–7141 (2018)
- [11] Ilg, E., Mayer, N., Saikia, T., Keuper, M., Dosovitskiy, A., Brox, T.: Flownet 2.0: Evolution of optical flow estimation with deep networks. In: Proceedings of the IEEE conference on computer vision and pattern recognition. pp. 2462–2470 (2017)
- [12] Jaderberg, M., Simonyan, K., Zisserman, A., et al.: Spatial transformer networks. In: Advances in neural information processing systems. pp. 2017–2025 (2015)
- [13] Jeon, Y., Kim, J.: Active convolution: Learning the shape of convolution for image classification. In: Proceedings of the IEEE Conference on Computer Vision and Pattern Recognition. pp. 4201–4209 (2017)
- [14] Jia, X., De Brabandere, B., Tuytelaars, T., Gool, L.V.: Dynamic filter networks. In: Advances in Neural Information Processing Systems. pp. 667–675 (2016)
- [15] Jiang, H., Sun, D., Jampani, V., Yang, M.H., Learned-Miller, E., Kautz, J.: Super slomo: High quality estimation of multiple intermediate frames for video interpolation. In: Proceedings of the IEEE Conference on Computer Vision and Pattern Recognition. pp. 9000–9008 (2018)
- [16] Kingma, D.P., Ba, J.: Adam: A method for stochastic optimization. *corr* abs/1412.6980 (2014) (2014)
- [17] Krizhevsky, A., Sutskever, I., Hinton, G.E.: Imagenet classification with deep convolutional neural networks. In: Advances in neural information processing systems. pp. 1097–1105 (2012)
- [18] LeCun, Y., Bottou, L., Bengio, Y., Haffner, P.: Gradient-based learning applied to document recognition. *Proceedings of the IEEE* **86**(11), 2278–2324 (1998)
- [19] Lee, H., Kim, T., Chung, T.y., Pak, D., Ban, Y., Lee, S.: Adacof: Adaptive collaboration of flows for video frame interpolation. In: Proceedings of the IEEE/CVF Conference on Computer Vision and Pattern Recognition. pp. 5316–5325 (2020)
- [20] Lin, T.Y., Dollár, P., Girshick, R., He, K., Hariharan, B., Belongie, S.: Feature pyramid networks for object detection. In: Proceedings of the IEEE conference on computer vision and pattern recognition. pp. 2117–2125 (2017)
- [21] Liu, X., Ma, Y., Shi, Z., Chen, J.: Griddehazenet: Attention-based multi-scale network for image dehazing. In: Proceedings of the IEEE International Conference on Computer Vision. pp. 7314–7323 (2019)
- [22] Liu, Z., Yeh, R.A., Tang, X., Liu, Y., Agarwala, A.: Video frame synthesis using deep voxel flow. In: Proceedings of the IEEE International Conference on Computer Vision. pp. 4463–4471 (2017)
- [23] Long, G., Kneip, L., Alvarez, J.M., Li, H., Zhang, X., Yu, Q.: Learning image matching by simply watching video. In: European Conference on Computer Vision. pp. 434–450. Springer (2016)
- [24] Meyer, S., Wang, O., Zimmer, H., Grosse, M., Sorkine-Hornung, A.: Phase-based frame interpolation for video. In: Proceedings of the IEEE conference on computer vision and pattern recognition. pp. 1410–1418 (2015)
- [25] Nah, S., Hyun Kim, T., Mu Lee, K.: Deep multi-scale convolutional neural network for dynamic scene deblurring. In: Proceedings of the IEEE Conference on Computer Vision and Pattern Recognition. pp. 3883–3891 (2017)
- [26] Niklaus, S., Liu, F.: Context-aware synthesis for video frame interpolation. In: Proceedings of the IEEE Conference on Computer Vision and Pattern Recognition. pp. 1701–1710 (2018)
- [27] Niklaus, S., Mai, L., Liu, F.: Video frame interpolation via adaptive convolution. In: Proceedings of the IEEE Conference on Computer Vision and Pattern Recognition. pp. 670–679 (2017)
- [28] Niklaus, S., Mai, L., Liu, F.: Video frame interpolation via adaptive separable convolution. In: Proceedings of the IEEE International Conference on Computer Vision. pp. 261–270 (2017)
- [29] Park, J., Woo, S., Lee, J.Y., Kweon, I.S.: Bam: Bottleneck attention module. *arXiv preprint arXiv:1807.06514* (2018)
- [30] Ranjan, A., Black, M.J.: Optical flow estimation using a spatial pyramid network. In: Proceedings of the IEEE Conference on Computer Vision and Pattern Recognition. pp. 4161–4170 (2017)
- [31] Ronneberger, O., Fischer, P., Brox, T.: U-net: Convolutional networks for biomedical image segmentation. In: International Conference on Medical image computing and computer-assisted intervention. pp. 234–241. Springer (2015)
- [32] Simonyan, K., Zisserman, A.: Very deep convolutional networks for large-scale image recognition. *arXiv preprint arXiv:1409.1556* (2014)
- [33] Soomro, K., Zamir, A.R., Shah, M.: Ucf101: A dataset of 101 human actions classes from videos in the wild. *arXiv preprint arXiv:1212.0402* (2012)
- [34] Su, S., Delbracio, M., Wang, J., Sapiro, G., Heidrich, W., Wang, O.: Deep video deblurring for hand-held cameras. In: Proceedings of the IEEE Conference on Computer Vision and Pattern Recognition. pp. 1279–1288 (2017)
- [35] Sun, D., Yang, X., Liu, M.Y., Kautz, J.: Pwc-net: Cnn for optical flow using pyramid, warping, and cost volume. In: Proceedings of the IEEE Conference on Computer Vision and Pattern Recognition. pp. 8934–8943 (2018)
- [36] Wang, T., Yang, X., Xu, K., Chen, S., Zhang, Q., Lau, R.W.: Spatial attentive single-image deraining with a high quality real rain dataset. In: Proceedings of the IEEE Conference on Computer Vision and Pattern Recognition. pp. 12270–12279 (2019)
- [37] Wang, X., Girshick, R., Gupta, A., He, K.: Non-local neural networks. In: Proceedings of the IEEE conference on computer vision and pattern recognition. pp. 7794–7803 (2018)
- [38] Woo, S., Park, J., Lee, J.Y., So Kweon, I.: Cbam: Convolutional block attention module. In: Proceedings of the European Conference on Computer Vision (ECCV). pp. 3–19 (2018)
- [39] Xu, X., Siyao, L., Sun, W., Yin, Q., Yang, M.H.: Quadratic video interpolation. In: NeurIPS (2019)
- [40] Xue, T., Chen, B., Wu, J., Wei, D., Freeman, W.T.: Video enhancement with task-oriented flow. *International Journal of Computer Vision* **127**(8), 1106–1125 (2019)
- [41] Zhang, Y., Tian, Y., Kong, Y., Zhong, B., Fu, Y.: Residual dense network for image super-resolution. In: Proceedings of the IEEE conference on computer vision and pattern recognition. pp. 2472–2481 (2018)
- [42] Zhao, H., Shi, J., Qi, X., Wang, X., Jia, J.: Pyramid scene parsing network. In: Proceedings of the IEEE conference on computer vision and pattern recognition. pp. 2881–2890 (2017)
- [43] Zhao, H., Zhang, Y., Liu, S., Shi, J., Change Loy, C., Lin, D., Jia, J.: Psanet: Point-wise spatial attention network for scene parsing. In: Proceedings of the European Conference on Computer Vision (ECCV). pp. 267–283 (2018)
- [44] Zhu, X., Hu, H., Lin, S., Dai, J.: Deformable convnets v2: More deformable, better results. In: Proceedings of the IEEE Conference on Computer Vision and Pattern Recognition. pp. 9308–9316 (2019)